

RF performance of top-gated, zero-bandgap graphene field-effect transistors

Inanc Meric¹, Natalia Baklitskaya¹, Philip Kim², and Kenneth L. Shepard¹

¹Department of Electrical Engineering, ²Department of Physics, Columbia University, New York, NY, 10027

Email: shepard@ee.columbia.edu

Abstract

We present the first experimental high-frequency measurements of graphene field-effect transistors (GFETs), demonstrating an f_T of 14.7 GHz for a 500-nm-length device. We also present detailed measurement and analysis of velocity saturation in GFETs, demonstrating the potential for velocities approaching 10^8 cm/sec and the effect of an ambipolar channel on current-voltage characteristics.

Introduction

Graphene, a two-dimensional sheet of carbon with a hexagonal lattice, offers many of the advantages of carbon nanotubes—carrier mobilities of up to 2×10^5 cm²/V-sec[1] and large ($\sim 10^8$ A/cm²) critical current densities[2]—without the need for assembling large parallel arrays of nanotubes to achieve high on currents. In graphene, the charge carriers in the two-dimensional channel can change from electrons to holes with the application of an electrostatic gate, with a minimum density (or Dirac) point characterizing the transition. Graphene is also characterized by a linear dispersion relation with the Dirac point separating the valence and conduction bands with no bandgap. This zero bandgap limits achievable on-off current ratios but this does not rule out analog/RF device applications.

In particular, there has been growing interest in graphene as a replacement for III-V materials in MMIC applications because of its high mobility, its potential for high saturation velocity, and its nearly perfect two-dimensional electrostatics. We have previously demonstrated some of the current-voltage properties of GFET devices[3]. In this paper, we present the first RF measurements of graphene field-effect transistors, demonstrating $f_T \approx 14.7$ GHz operation of 500-nm-length devices. The saturation velocity (v_{sat}) is sheet-carrier dependent and limited by the Fermi velocity, $v_F = 10^8$ cm/sec. Interfacial phonon scattering from the SiO₂ substrate upon which the graphene is fabricated limits v_{sat} .

Device Fabrication

Fig. 1 shows the basic structure of a graphene field-effect transistors (GFETs), GFET A has a ground-signal-ground probe structure to support RF measurement. In addition, we present DC characteristics of a second device, GFET B,

which cannot support RF measurement, but which has superior device characteristics. Fabrication starts with mechanically exfoliated graphene[4] from Kish graphite on a high-resistivity Si substrate ($\rho = 20,000$ Ω -cm) with a 300-nm thermally grown SiO₂ layer; the substrate, though highly resistive, still functions as a back-gate. Single-layer graphene pieces are identified optically and confirmed with Raman spectroscopy. Source/drain electrodes are patterned onto the selected graphene pieces with electron-beam lithography followed by a Cr/Au (3 nm/80 nm) deposition. A 30-nm HfO₂ film is directly grown with atomic layer deposition (ALD) at 90 °C as the top-gate dielectric on the active device area, followed by the patterning of a Cr/Au gate. GFET A (Fig. 1) has two fingers of W/L = 2.5 μ m/0.5 μ m while GFET B has a single W/L = 2.1 μ m/1 μ m finger. The source/drain separation is 3 μ m in both devices. The global back-gate controls the resistance of the resulting “spacer” regions outside the active channel.

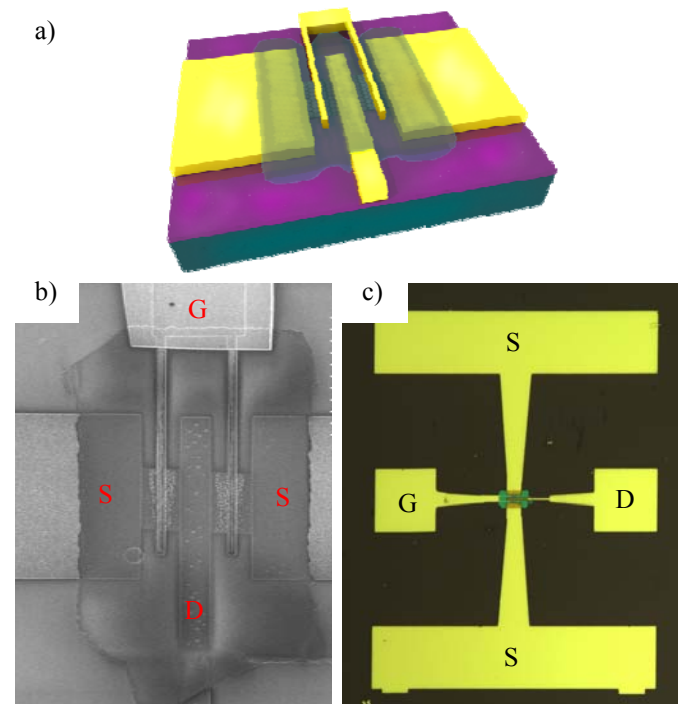


Fig.1 Graphene FET structure. (a) schematic depiction of the GFET on a Si/SiO₂ substrate; (b) SEM micrograph of the graphene transistor; (c) image of the entire probed RF device structure.

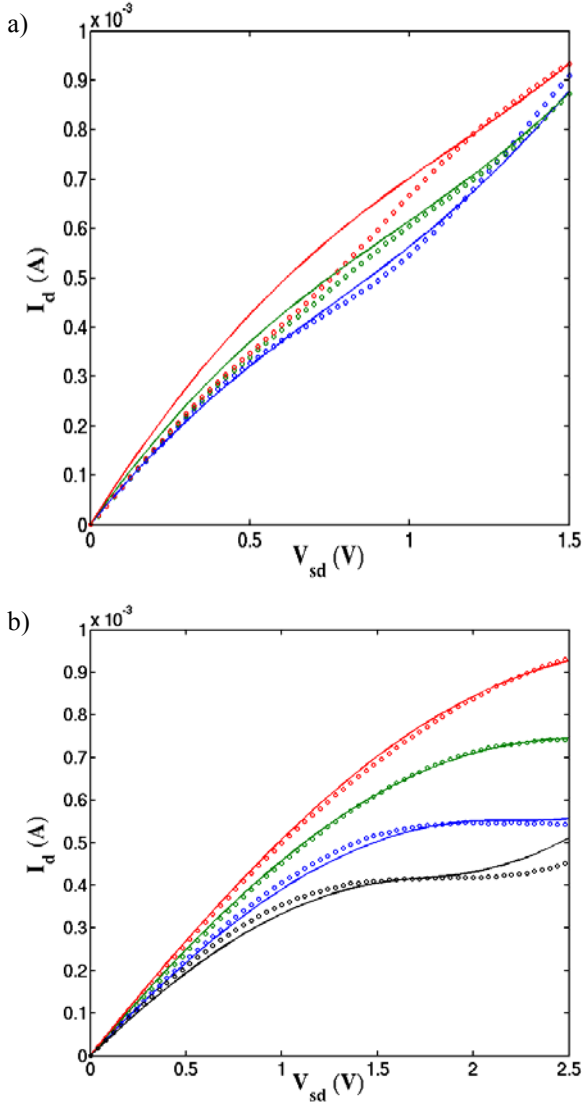


Fig. 2 Current-voltage characteristics of GFET device. Drain current (I_d) as a function of source-to-drain voltage (V_{sd}) for a) GFET A at $V_{gs-top} = -0.1V, -0.3V, -0.5V$ and for b) GFET B $V_{gs-top} = 0V, -0.5V, -1.5V, -2.5V$ (from bottom to top). Both measured (solid curves) and simulated (dashed curves) results are shown.

Device I-V Characterization

DC measurements are carried out in ambient conditions with an Agilent 4155C. Fig. 2a shows the measured I-V characteristics of GFET A, while Fig. 2b shows the comparable characteristics for GFET B. Sheet carrier concentrations (electrons or holes) in the source and drain regions are given by

$$n \cong \sqrt{n_0^2 + (C_{back}(V_{gs-back} - V_{gs-back}^0)/e)^2}, \quad \text{where}$$

$V_{gs-back}^0$ is the back-gate-to-source voltage at the Dirac point in these regions and n_0 is the minimum sheet carrier concentration as determined by disorder and thermal excitation. C_{back} , the back-gate capacitance, is approximately 12 nF/cm^2

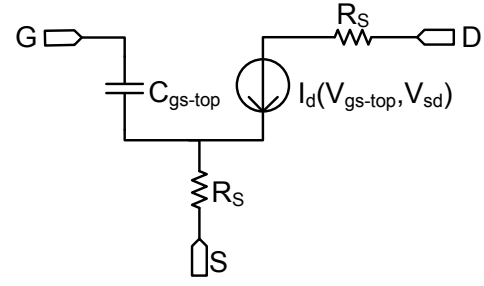


Fig. 3 Compact model of graphene FET. $I_d(V_{sd}, V_{gs-top})$ is given by the equations of Table I.

for both GFETs. Under the top gate, carrier concentrations are determined by both the front and back gates, $n = \sqrt{n_0^2 + (C_{top}(V_{gs-top} - V_0)/e)^2}$, where V_0 , which has the character of a threshold voltage, is given by $V_0 \cong V_{gs-top}^0 + (C_{back}/C_{top})(V_{gs-back}^0 - V_{gs-back})$. C_{top} , given by the parallel combination of the electrostatic capacitance of the gate and the quantum capacitance of graphene (which ultimately limits achievable gate capacitances) is 382 nF/cm^2 (552 nF/cm^2) for GFET A(B) due to different oxide thicknesses.

One of the interesting features of these characteristics is the “kink” observed most notably for $V_{gs-top} = 0 \text{ V}$ for GFET B. As V_{sd} increases beyond the “kink” voltage ($V_{sd-kink} = V_{gs-top} - V_0$) the channel transitions from being all holes to being ambipolar with electrons at the drain and, therefore, with the Dirac point positioned in the channel. In this ambipolar regime, the Dirac point becomes a place of recombination for holes flowing from the source and electrons flowing from the drain. Because there is no bandgap, no energy is released in this recombination. For optimal high-frequency operation, the ambipolar regime has to be kept outside the channel by the proper choice of V_0 and biasing. In the unipolar regime ($V_{sd} < V_{sd-kink}$), GFET B shows saturating I-V characteristics. To model this effect, the drift velocity of the carriers must be assumed to saturate.

Fig. 2 also shows the results of simple field-effect modeling of the devices. This field-effect model shown in Fig. 3 is implemented in Verilog-A with the equations of Table I. R_s is approximately 100Ω (700Ω) for GFET A(B). GFET A has a low-field mobility $\mu = 105 \text{ cm}^2/V \text{ sec}$ and $n_0 = 5 \times 10^{12} \text{ cm}^{-2}$, compared with $\mu = 1200 \text{ cm}^2/V \text{ sec}$ and $n_0 = 0.5 \times 10^{12} \text{ cm}^{-2}$ for GFET B. Because of this degraded mobility, $V_{sd-kink} < v_{sat}L/\mu$ for GFET A and the device does not show significant velocity saturation.

The saturation velocity (v_{sat}) depends on carrier concentration in this model with $v_{sat} = v_F(\beta/\sqrt{n} + \alpha)$, where $\alpha \approx -0.07$ and $\beta \approx 0.4 \times 10^6 \text{ cm}^{-1}$ as shown in Fig. 4 for GFET B. This carrier concentration dependence can be explained by a

TABLE I

Current-voltage equation derivation for the GFET

$$I_d = \frac{W}{L} \int_0^L en(x)v_{drift}(x)dx \quad (1)$$

$$v_{drift} = \frac{\mu E}{1 + \frac{\mu E}{v_{sat}}} \quad (2)$$

$$n(x) = \sqrt{n_0^2 + \left(\frac{C_{top}(V_{gs-top} - V(x) - V_0)}{e}\right)^2} \quad (3)$$

$$I_d = \frac{W e \mu \int_0^{V_{sd}} \sqrt{n_0^2 + (C_{top}(V_{gs-top} - V - V_0)/e)^2} dV}{1 + \frac{\mu V_{sd}}{L v_{sat}}} \quad (4)$$

Combining Eqns. 1-3 yields Eqn. 4. μ is the low-field mobility, $E = -dV/dx$ the electric field along the channel, v_{sat} the saturation velocity, n_0 the carrier concentration (electrons and holes) at the Dirac point due to disorder, and R_s the source-drain parasitic series resistances.

simple model in which one assumes strong coupling of the carriers to phonons with an energy $\hbar\Omega$. In this case, one can show that $v_{sat} = v_F(\hbar\Omega/E_F)$ (for $\hbar\Omega \ll E_F$) with E_F given by $E_F = \hbar v_F \sqrt{\pi n}$ [3]. The constant term α models the empirical fact that v_{sat} modeled by the simple phonon emission model overestimates the saturation velocity. From the carrier-concentration dependence of v_{sat} , we find $\hbar\Omega \approx 50$ meV, comparable to the surface phonon energy of SiO₂[5]. This suggests that saturation velocities approaching the Fermi velocity of 1×10^8 cm/sec could be possible with a proper substrate choice.

Fig. 5 shows the measured small-signal device transconductance, g_m , for both devices. g_m has a pronounced

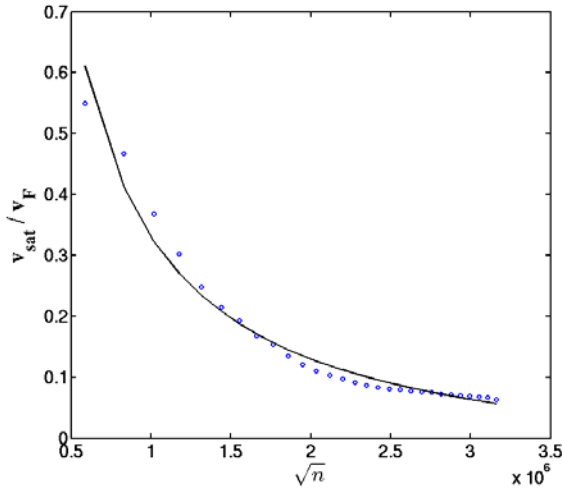


Fig. 4 Fermi energy dependence of the saturation velocity. v_{sat} as function of carrier concentration for the data of Fig. 2. The slope corresponds to a phonon energy of ≈ 50 meV.

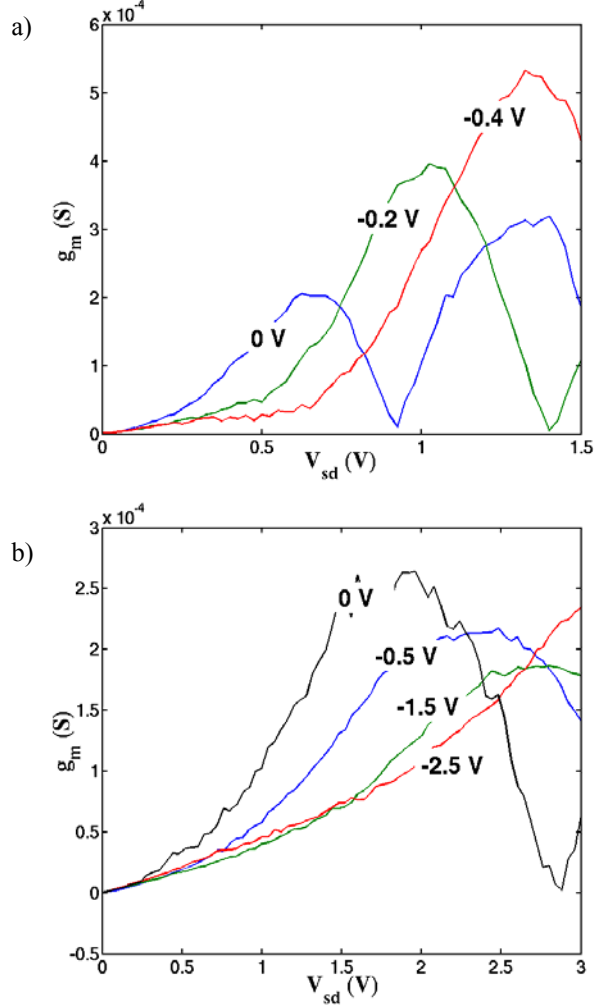


Fig. 5 Small-signal transconductance (g_m) as a function of drain-to-source voltage (V_{sd}) for a) GFET A at $V_{gs-top} = -0.1V, -0.3V, -0.5V$ and b) GFET B $V_{gs-top} = 0V, -0.5V, -1.5V, -2.5V$.

zero at $V_{sd-kink}$. The highest transconductances are observed in the unipolar regime away from $V_{sd-kink}$, which can be achieved by proper choice of V_0 . Therefore the device is most likely to be operated in the high-transconductance, velocity-saturated region with V_{sd} below $V_{sd-kink}$.

Device Frequency Response

S-parameter characterization of the GFET A device in the 50 MHz to 20 GHz range is carried out with on-wafer probes and an Agilent N5230A PNA-L network analyzer. An “open” de-embedding structure is measured and used to remove the effects of pad parasitic using a y-parameter de-embedding procedure. The S-parameters of the GFET are measured at $V_{gs-back} = -15$ V, $V_{gs-top} = -0.25$ V, and $V_{sd} = 1.5$ V. Fig. 6 shows the frequency response of the small-signal current gain h_{21} , giving a unity-gain frequency (f_T) of 14.7 GHz.

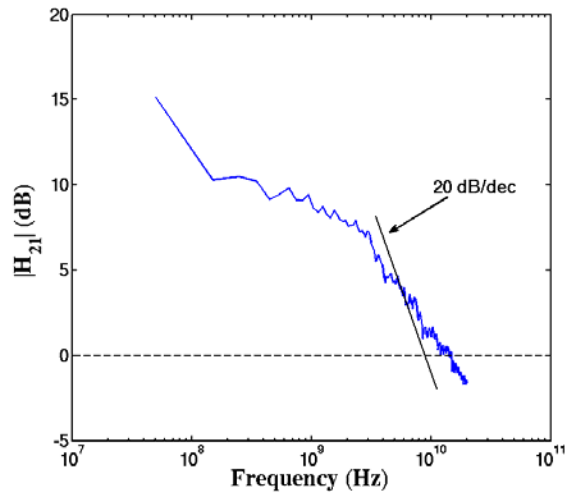


Fig. 5 h_{21} frequency response. Measured forward current gain of GFET B after deembedding of pad parasitics.

The measured device $f_T = g_m / 2\pi C_g$ is consistent with a measured g_m of 550 μS and C_g of 5.95 fF. Because of the high g_{ds} and poor R_s of GFET A at this bias point, $f_{max} < 1 \text{ GHz}$. We are seeking to fabricate a velocity-saturated GFET B device in an RF layout, which should have f_T performance of more than 40 GHz at the same channel length.

Conclusion

In this work, we have fabricated and measured the first RF GFET device, yielding f_T performance exceeding 14 GHz for a 500-nm-length channel. We have elucidated unique fea-

tures in the current-voltage characteristics of these devices that result from an ambipolar channel and concentration-dependent saturation velocities. Further progress in the reproducibility of device fabrication should result in rapid measured performance increases. Wider device structures will also be necessary for noise figure characterization and to utilize these devices in simple RF circuits, such as low-noise amplifiers (LNAs).

Acknowledgement

This work was supported by the Focus Center Research Program (FCRP) through the Center for Circuits and Systems Solutions (C2S2) and the Center on Functional Engineered Nano Architectonics (FENA).

References

- [1] K. I. Bolotin, et al., "Ultrahigh electron mobility in suspended graphene," *Solid State Communications*, vol. 146, pp. 351-355, 2008.
- [2] K. S. Novoselov, et al., "Two-dimensional gas of massless Dirac fermions in graphene," *Nature*, vol. 438, pp. 197-200, 2005.
- [3] I. Meric, M. Y. Han, A. F. Young, B. Ozyilmaz, P. Kim, and K. L. Shepard, "Current saturation in zero-bandgap, top-gated graphene field-effect transistors," *Nature Nanotechnology*, 2008. DOI:10.1038/nnano.2008.268
- [4] K. S. Novoselov, et al., "Electric Field Effect in Atomically Thin Carbon Films," *Science*, vol. 306, pp. 666-669, 2004.
- [5] J.-H. Chen, C. Jang, S. Xiao, M. Ishigami, and M. S. Fuhrer, "Intrinsic and extrinsic performance limits of graphene devices on SiO₂," *Nat Nanotechnology*, vol. 3, pp. 206-209, 2008.